

New mass-loss rates of Magellanic Cloud B supergiants from global wind models

J. Krtička¹, J. Kubát², and I. Krtičková¹

¹ Department of Theoretical Physics and Astrophysics, Faculty of Science, Masaryk University, CZ-611 37 Brno, Czech Republic

² Astronomical Institute, Czech Academy of Sciences, CZ-251 65 Ondřejov, Czech Republic

Received

ABSTRACT

We provide global models of line-driven winds of B supergiants for metallicities corresponding to the Large and Small Magellanic Clouds. The velocity and density structure of the models is determined consistently from hydrodynamical equations with radiative force derived in the comoving frame and level populations computed from kinetic equilibrium equations. We provide a formula expressing the predicted mass-loss rates in terms of stellar luminosity, effective temperature, and metallicity. Predicted wind mass-loss rates decrease with decreasing metallicity as $\dot{M} \sim Z^{0.60}$ and are proportional to the stellar luminosity. The mass-loss rates increase below the region of the bistability jump at about 20 kK because of iron recombination. In agreement with previous theoretical and observational studies, we find a smooth change of wind properties in the region of the bistability jump. With decreasing metallicity, the bistability jump becomes weaker and shifts to lower effective temperatures. At lower metallicities above the bistability jump, our predictions provide similar rates to those used in current evolutionary models, but our rates are significantly lower than older predictions below the bistability jump. Our predicted mass-loss rates agree with observational estimates derived from H α line assuming that observations of stellar winds from Galaxy and the Magellanic Clouds are uniformly affected by clumping. The models nicely reproduce the dependence of terminal velocities on temperature derived from ultraviolet spectroscopy.

Key words. stars: winds, outflows – stars: mass-loss – stars: early-type – supergiants – hydrodynamics – Magellanic Clouds

1. Introduction

The stellar winds of hot stars are accelerated by the radiative force mainly due to line transitions of heavy elements. Thanks to their resonance character, line transitions due to bound electrons can be much more efficient in radiative acceleration than scattering on free electrons (Gayley 1995). However, the line interaction is confined to a relatively narrow range of frequencies given by line broadening. This is the place where the Doppler effect comes into play, which enables a given line to cover a much larger portion of the stellar flux than just the confined range of frequencies given by the line broadening (Milne 1926).

Trace elements heavier than hydrogen and helium are the most effective in absorbing stellar radiation and in accelerating the wind. Therefore, the process of Coulomb collision between charged particles is needed to accelerate the bulk of the wind material composed of hydrogen and helium (Castor et al. 1976; Springmann & Pauldrach 1992; Krtička et al. 2003).

As a result of the dependence of the radiative force on the wind chemical composition, the amount of mass lost by the star per unit of time, that is, the wind mass-loss rate \dot{M} , scales with metallicity (Vink et al. 2001; Krtička & Kubát 2018; Björklund et al. 2021). In general, the winds are the strongest at high metallicities and cease at zero metallicity (Krtička & Kubát 2006). Therefore, in addition to luminosity and effective temperature, metallicity is one of the main parameters that determine the wind mass-loss rate.

The metallicity dependence of wind strength becomes important in galaxies that have different star formation histories from that of our Galaxy. The Magellanic Clouds are typical examples of such galaxies, which, thanks to their lower metal-

licity (e.g., Hill et al. 1995; Venn 1999; Rolleston et al. 2002; Bouret et al. 2003) and relative proximity, provide an important benchmark for the study of evolution of stars and their interaction with the circumstellar environment. The Large and Small Magellanic Clouds (LMC and SMC, respectively) are galaxies that gravitationally interact with our Galaxy and the LMC is still likely completing its first orbit around the Milky Way (Patel et al. 2017). The LMC is massive enough to significantly perturb the orbits of the satellites of our Galaxy (Battaglia et al. 2022). The Magellanic Clouds have a complex star formation history, with several synchronized peaks having taken place over the last few billion years (Weisz et al. 2013; Massana et al. 2022).

Mass loss influences the evolution of stars (Keszthelyi et al. 2017) and their interaction with the interstellar environment (Kobulnicky et al. 2019), which can leave impacts on future stellar generations (Szécsi & Wunsch 2019). Therefore, reliable estimates of mass-loss rates are required in order to understand the physics of stars and of the interstellar medium. This becomes especially appealing when significantly lower wind mass-loss rates are predicted from global wind models of massive stars (Krtička & Kubát 2017; Sander et al. 2017; Björklund et al. 2021). These models solve the radiative transfer equation precisely in the comoving frame and allow a smooth transition from photosphere to the wind. The suggested reduction in mass-loss rates seems to be in line with a more precise observational analysis taking into account the effect of wind inhomogeneities (Najarro et al. 2011; Bouret et al. 2012; Šurlan et al. 2013).

Here, we provide new mass-loss rate estimates for B supergiants for metallicities corresponding to the Magellanic Clouds.

These models complement our previous grids computed for B supergiants from our Galaxy (Krtićka et al. 2021) and for O stars from the Magellanic Clouds (Krtićka & Kubát 2018) and our Galaxy (Krtićka & Kubát 2017). Our models provide an alternative prescription to that of Björklund et al. (2023). The mass-loss-rate prescriptions given in Krtićka & Kubát (2018) and Krtićka et al. (2021) yield a reasonably good fit for most blue supergiant stars analyzed by Bernini-Peron et al. (2023) and for stars from the Large Magellanic Cloud cluster R136 (Brands et al. 2022).

2. Wind modeling of LMC and SMC B supergiants

We used the code METUJE, which was applied by Krtićka et al. (2021) in the modeling of Galactic B supergiants. The adopted assumptions were described by Krtićka & Kubát (2017) in detail. The code provides spherically symmetric and stationary models of the line-driven stellar wind by solving hydrodynamical equations together with radiative transfer and kinetic equilibrium equations. The equations are solved in a global manner, that is, from nearly hydrostatic photosphere to supersonically expanding wind. The output of the model calculations provides radial variations of structural parameters, including wind velocity, density, temperature, and level populations. Our approach is similar to using other codes that provide consistent hydrodynamical models of hot star winds (Gräfener & Hamann 2008; Sander et al. 2017; Sundqvist et al. 2019).

Level occupation numbers of model ions are determined from the kinetic equilibrium equations. These equations account for bound–bound, bound–free, and Auger transitions between individual levels. We either adopted the models of ions from the TLUSTY model input data (Lanz & Hubeny 2003, 2007) or prepared them ourselves using data from the Opacity and Iron Projects (Seaton et al. 1992; Hummer et al. 1993) and the NIST database (Kramida et al. 2015).

The derived level populations enter the absorption and emission terms in the radiative transfer equation, which is solved in the comoving frame (CMF; Mihalas et al. 1975). The derived radiation field is used to determine the radiative force and radiative heating and cooling terms, which are included in equation of motion and in energy equations. These hydrodynamical equations are supplemented with the continuity equation and yield the radial profiles of velocity, density, and temperature of the wind.

All equations are solved iteratively, which allows us to derive a consistent flow structure. The models are parameterized by basic stellar parameters, that is, the stellar effective temperature T_{eff} , stellar mass M , radius R_* , and surface chemical composition. The main output parameters are wind mass-loss rate \dot{M} and terminal wind velocity v_∞ .

Hot star winds show signatures of small-scale structure (clumping) in their spectra (Sundqvist et al. 2010; Šurlan et al. 2012; Flores et al. 2023). Such inhomogeneities probably originate from line-deshadowing instability (Feldmeier & Thomas 2017; Sundqvist et al. 2018). To understand the effect of inhomogeneities, we calculated an additional set of models that account for clumping (as in, e.g., Krtićka et al. 2018). We assumed optically thin clumping parameterized by a clumping factor $C_c = \langle \rho^2 \rangle / \langle \rho \rangle^2$. Here, the angle brackets denote the average over volume. We adopted an empirically motivated radial-dependent clumping factor (Najarro et al. 2009; Bouret et al. 2012):

$$C_c(r) = C_1 + (1 - C_1) e^{-\frac{v(r)}{C_2}}, \quad (1)$$

which grows from $C_c = 1$ (corresponding to smooth wind) to C_1 for velocities higher than C_2 . We selected $C_1 = 10$, which is

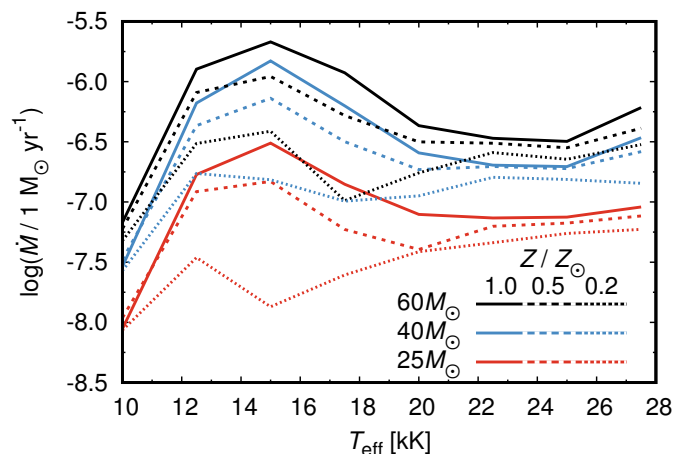


Fig. 1. Predicted mass-loss rate as a function of effective temperature. Line color denotes stellar mass (or luminosity) and line type encodes metallicity, with solid lines corresponding to Z_\odot , dashed lines to $0.5 Z_\odot$, and dotted lines to $0.2 Z_\odot$.

roughly the value at which the empirical $H\alpha$ mass-loss rates of O stars agree with other estimates (Krtićka & Kubát 2017) and $C_2 = 100 \text{ km s}^{-1}$, which is typically derived from the observational study of Bouret et al. (2012). The radial velocity variation $v(r)$ in Eq. (1) is approximated by the fit of the wind velocity determined for the unclumped wind ($C_c = 1$) by a polynomial formula provided by Krtićka & Kubát (2011), which was modified to

$$\tilde{v}(r) = \sum_i v_i \left(1 - \gamma \frac{R_*}{r}\right)^i, \quad (2)$$

where v_i and γ are parameters of the fit.

3. Calculated wind models

The models were calculated for the same grid of stellar parameters as in Krtićka et al. (2021). The parameters given in Table 1 cover the spectral range of B supergiants at three different values of stellar luminosity L . The adopted parameters correspond to typical values determined for B supergiants from observations in Crowther et al. (2006). To account for a typical chemical composition of the LMC and SMC (e.g., Hill et al. 1995; Venn 1999; Rolleston et al. 2002; Bouret et al. 2003), we calculated two sets of models with solar chemical composition Z_\odot (Asplund et al. 2009) scaled by a factor of 0.5 or 0.2 for elements heavier than helium.

The resulting wind parameters are given in Table 1 for these two selected metallicities. The parameters are compared to predictions derived for Galactic B supergiants (Krtićka et al. 2021) and are given for a smooth wind with $C_1 = 1$ and for a clumped wind with $C_1 = 10$. The parameters of the fit of the velocities in Eq. (2) —used to calculate clumped models— are given in Table 2.

From Fig. 1 and Table 1, it follows that the mass-loss rate increases with increasing luminosity and metallicity. On average, the mass-loss rates of B supergiants increase with metallicity as $\dot{M} \sim Z^{0.60}$. The temperature variations are more complex. The mass-loss rate slightly decreases with decreasing temperature down to about 22 kK because of the declining flux in the ultraviolet domain, where the lines accelerating the wind mostly

Table 1. Stellar parameters of the model grid with derived values of the terminal velocity v_∞ (in km s^{-1}) and the mass-loss rate \dot{M} (in $M_\odot \text{ yr}^{-1}$).

Model	T_{eff} [kK]	R_* [R_\odot]	$Z = Z_\odot$		$Z = 0.5 Z_\odot$				$Z = 0.2 Z_\odot$			
			$C_1 = 1$	$C_1 = 10$	$C_1 = 1$	$C_1 = 10$	$C_1 = 1$	$C_1 = 10$	$C_1 = 1$	$C_1 = 10$		
$M = 25 M_\odot, \log(L/L_\odot) = 5.28, \Gamma = 0.18$												
275-25	27.5	19.3	1890	9.1×10^{-8}	1920	7.7×10^{-8}	2040	8.4×10^{-8}	1880	5.9×10^{-8}	2090	6.5×10^{-8}
250-25	25.0	23.3	1640	7.5×10^{-8}	1540	6.7×10^{-8}	1730	7.4×10^{-8}	1340	5.5×10^{-8}	1750	5.5×10^{-8}
225-25	22.5	28.8	1130	7.4×10^{-8}	1060	6.3×10^{-8}	1300	7.3×10^{-8}	1240	4.6×10^{-8}	1500	5.1×10^{-8}
200-25	20.0	36.4	760	7.9×10^{-8}	1520	4.0×10^{-8}	960	1.3×10^{-7}	1220	3.9×10^{-8}	960	5.2×10^{-8}
175-25	17.5	47.6	570	1.4×10^{-7}	380	5.9×10^{-8}	820	1.9×10^{-7}	1020	2.5×10^{-8}	720	7.5×10^{-8}
150-25	15.0	64.8	510	3.1×10^{-7}	470	1.5×10^{-7}	510	2.6×10^{-7}	1050	1.3×10^{-8}	670	4.5×10^{-8}
125-25	12.5	93.3	120	1.7×10^{-7}	130	1.2×10^{-7}	120	1.3×10^{-7}	120	3.5×10^{-8}	130	4.7×10^{-8}
100-25	10.0	146	480	8.8×10^{-9}	410	1.1×10^{-8}	430	1.1×10^{-8}	360	8.6×10^{-9}	430	9.6×10^{-9}
$M = 40 M_\odot, \log(L/L_\odot) = 5.66, \Gamma = 0.27$												
275-40	27.5	29.9	1300	3.4×10^{-7}	1510	2.6×10^{-7}	1370	3.1×10^{-7}	1670	1.4×10^{-7}	1960	2.0×10^{-7}
250-40	25.0	36.1	1600	2.0×10^{-7}	1320	1.9×10^{-7}	1610	2.1×10^{-7}	1170	1.5×10^{-7}	1500	1.6×10^{-7}
225-40	22.5	44.6	1160	2.0×10^{-7}	880	2.0×10^{-7}	820	2.7×10^{-7}	860	1.6×10^{-7}	1220	1.7×10^{-7}
200-40	20.0	56.4	700	2.6×10^{-7}	670	1.9×10^{-7}	1100	4.6×10^{-7}	930	1.1×10^{-7}	890	1.9×10^{-7}
175-40	17.5	73.7	630	6.3×10^{-7}	580	3.2×10^{-7}	520	8.6×10^{-7}	530	1.0×10^{-7}	780	2.8×10^{-7}
150-40	15.0	100	110	1.5×10^{-6}	90	7.3×10^{-7}	110	1.2×10^{-6}	60	1.5×10^{-7}	80	5.0×10^{-7}
125-40	12.5	145	80	6.6×10^{-7}	100	4.3×10^{-7}	100	4.7×10^{-7}	70	1.7×10^{-7}	110	1.9×10^{-7}
100-40	10.0	226	410	2.9×10^{-8}	410	3.3×10^{-8}	440	3.4×10^{-8}	400	2.7×10^{-8}	410	2.7×10^{-8}
$M = 60 M_\odot, \log(L/L_\odot) = 5.88, \Gamma = 0.30$												
275-60	27.5	38.5	1240	6.1×10^{-7}	1680	4.1×10^{-7}	1520	4.9×10^{-7}	1910	3.0×10^{-7}	1930	3.6×10^{-7}
250-60	25.0	46.5	1850	3.2×10^{-7}	1780	2.8×10^{-7}	1720	3.4×10^{-7}	1520	2.3×10^{-7}	1860	2.5×10^{-7}
225-60	22.5	57.5	1000	3.4×10^{-7}	880	3.1×10^{-7}	1310	4.6×10^{-7}	940	2.6×10^{-7}	1250	2.8×10^{-7}
200-60	20.0	72.7	760	4.3×10^{-7}	650	3.2×10^{-7}	1230	8.8×10^{-7}	1170	1.7×10^{-7}	1080	2.7×10^{-7}
175-60	17.5	95.0	820	1.2×10^{-6}	650	5.2×10^{-7}	800	1.4×10^{-6}	1570	1.0×10^{-7}	940	2.4×10^{-7}
150-60	15.0	129	490	2.1×10^{-6}	540	1.1×10^{-6}	530	1.6×10^{-6}	460	3.9×10^{-7}	580	4.9×10^{-7}
125-60	12.5	186	110	1.3×10^{-6}	150	8.1×10^{-7}	140	8.9×10^{-7}	130	3.1×10^{-7}	140	3.8×10^{-7}
100-60	10.0	291	120	6.8×10^{-8}	120	6.0×10^{-8}	120	6.2×10^{-8}	130	4.8×10^{-8}	110	4.5×10^{-8}

Notes. Γ is the Eddington parameter for electron Thomson scattering opacity.

appear. Below this temperature, the mass-loss rates start to gradually increase by a factor of a few. This rise is referred to as a bistability jump (Pauldrach & Puls 1990), and is caused by the recombination of iron from Fe IV to Fe III (Vink et al. 1999; Vink 2018; Krtićka et al. 2021). The change in the efficiency of wind acceleration is connected to the fact that ions with lower charge have typically more lines at longer wavelengths close to the stellar flux maximum.

These effects are also demonstrated in Fig. 2, which plots the contribution of selected elements to the radiative force as a function of effective temperature. In comparison with Fig. 2 in Krtićka et al. (2021), we do not plot the elements with a relatively low contribution (Al, P, and S). For the hottest stars, the radiative force is dominated by elements lighter than iron. With decreasing temperature the wind recombines and the radiative driving becomes dominated by iron for $T_{\text{eff}} < 15$ kK. However, due to lower iron abundance, with decreasing metallicity the iron lines become optically thin and contribute to the radiative force to a lesser extent. As a result, the bistability jump weakens with lower metallicity (as found by Vink et al. 2001) and becomes apparent only when Fe III dominates for $T_{\text{eff}} < 15$ kK.

The predicted mass-loss rates of OB supergiants and main sequence O stars, and giants from the Galaxy and the Magellanic Clouds without clumping (Krtićka & Kubát 2017, 2018;

Krtićka et al. 2021), can be fitted via

$$\log\left(\frac{\dot{M}}{1 M_\odot \text{ yr}^{-1}}\right) = a + \alpha \log\left(\frac{Z}{Z_\odot}\right) + \left[b + \beta \log\left(\frac{Z}{Z_\odot}\right)\right] \log\left(\frac{L}{10^6 L_\odot}\right) - a \log\left\{\left[1 + \delta \log\left(\frac{Z}{Z_\odot}\right)\right] \exp\left[-\frac{(T_{\text{eff}} - T_1)^2}{\Delta T_1^2}\right] + c \exp\left[-\frac{(T_{\text{eff}} - T_2)^2}{\Delta T_2^2}\right]\right\}. \quad (3)$$

Here, \log denotes logarithm with base 10 and \exp denotes the natural exponential. Derived parameters of the fit are given in Table 3. The fit approximates the predicted mass-loss rates with a typical error of about 20 %. The error is slightly higher in the B supergiant domain. The fit Eq. (3) uses a Gaussian function to depict the temperature modulation of the mass-loss rates, and therefore it cannot be applied outside the fitted T_{eff} domain, which is 10 – 45 kK. Application of Eq. (3) for luminosities and metallicities significantly outside the domain for which we obtained the fit, that is, $\log(L/L_\odot) = 5.28 - 5.88$ and $Z/Z_\odot = 0.2 - 1.0$, could also lead to spurious results.

In addition to the discussed dependence of the mass-loss rate on the stellar luminosity, effective temperature, and metallicity, Eq. (3) introduces scaling of luminosity and temperature dependencies with the metallicity via parameters β and δ .

Table 2. Parameters of the fit of the wind radial velocity of unclumped model (Eq. (2)).

Model	0.5 Z_{\odot}				0.2 Z_{\odot}			
	v_1	v_2	v_3	γ	v_1	v_2	v_3	γ
	[km s $^{-1}$]				[km s $^{-1}$]			
275-25	3720	-1652		1.042	3508	-1549		1.044
250-25	4694	-3631		1.045	3812	-2771		1.044
225-25	3608	-3161		1.059	1853	-597		1.040
200-25	2105	-493		1.043	1143	244		1.039
175-25	836	-293		1.064	2014	-781		1.072
150-25	646	-92		1.069	2603	-1620		1.101
125-25	567	-1117	797	1.078	437	-775	500	1.076
100-25	790	-346		1.129	440	-35		1.111
275-40	2380	-620		1.056	3954	-2269		1.069
250-40	3519	-2256		1.058	3836	-3238		1.057
225-40	2663	-2021		1.065	2496	-1907		1.059
200-40	1659	-1043		1.070	1527	-419		1.064
175-40	790	-91		1.074	848	-48		1.076
150-40	724	-1891	1532	1.093	630	-2454	3276	1.096
125-40	625	-1635	1519	1.103	779	-3351	5345	1.115
100-40	763	-321		1.155	537	-106		1.149
275-60	2629	-753		1.057	2723	-568		1.059
250-60	4737	-3096		1.066	4854	-3956		1.062
225-60	2731	-2155		1.062	2465	-1675		1.052
200-60	1770	-1200		1.068	1392	94		1.061
175-60	851	-98		1.069	2471	-688		1.092
150-60	808	-168		1.075	635	-78		1.075
125-60	539	-939	598	1.084	502	-932	620	1.100
100-60	619	-1363	1081	1.126	505	-902	603	1.124

Table 3. Parameters of the fit of the mass-loss rate in Eq. (3).

a	b	c	T_1	T_2	ΔT_1	ΔT_2	α	β	δ
			[kK]	[kK]	[kK]	[kK]			
-13.82	1.52	3.84	14.16	37.90	3.58	56.5	0.358	-0.11	0.73

The temperature dependence is modified only below the bistability jump thanks to the absence of metallicity in the very last term of Eq. (3). These modifications lead to a steeper dependence of the mass-loss rate on luminosity for lower metallicities and to a weaker bistability jump at low metallicities. The modification of the luminosity dependence of the mass-loss rate with metallicity is very similar to that introduced by Krtićka & Kubát (2018), who interpreted the modification in terms of weaker blocking of far-UV flux at low metallicity and by a variation of the slope of the line-strength distribution function (Puls et al. 2000) with metallicity. The weakening of the bistability jump at low metallicities is connected to the lower contribution of iron to the radiative force for lower metallicities (Fig. 2, also Vink et al. 2001). Björklund et al. (2023) introduced an additional modification of temperature variations with metallicity that can mimic luminosity variations in Eq. (3), albeit with stronger effect. Analogous but steeper metallicity variations were found by Gormaz-Matamala et al. (2022). Vink & Sander (2021) predict the metallicity dependence of mass-loss rates as $\dot{M} \sim Z^{0.42}$ above the bistability jump and $\dot{M} \sim Z^{0.85}$ below the jump. For a typical luminosity in their work, $\log(L/L_{\odot}) = 5.5$, Eq. (3) predicts very similar scaling $\dot{M} \sim Z^{0.41}$ above the jump and a dependence below the jump that is stronger by a factor of a few.

As a result of clumping, the matter density in clumps becomes higher than the density in a smooth wind. For optically thin clumping, this leads to stronger recombination

(Hamann & Koesterke 1998; Bouret et al. 2003; Martins et al. 2005; Puls et al. 2006). Because ions with lower charge are typically able to drive wind more efficiently, with stronger clumping the mass-loss rate increases (Table 1). Typically, the increase is relatively small, but this effect intensifies in the region of the bistability jump. As a result of clumping, the bistability jump shifts towards higher effective temperatures. This leads to a more significant increase in the mass-loss rate by a factor of up to three, which corresponds to a proportionality of $\dot{M} \sim C_c^{0.5}$ there. Outside the region of the bistability jump (for $T_{\text{eff}} \geq 22.5$ kK or $T_{\text{eff}} \leq 12.5$ kK), the increase in the mass-loss rate is lower, of namely about 1.14, corresponding to $\dot{M} \sim C_c^{0.06}$.

Wind theory predicts that the terminal velocities scale mostly with surface escape speed (Castor et al. 1975). In our sample of stars with constant luminosities, radius increases with decreasing effective temperature, and therefore the scaling of the terminal velocities with escape speed leads to a decrease in terminal velocity with temperature (Table 1). The terminal velocities additionally significantly decrease in the region of the bistability jump (Vink 2018; Krtićka et al. 2021), which can be interpreted in terms of a varying line-strength distribution function (Puls et al. 2000; Krtićka et al. 2021). The terminal velocities increase again around $T_{\text{eff}} \approx 10$ kK as a result of the lower importance of iron for line driving. We did not find any strong dependence of terminal velocity on metallicity, except the slight shift of the bistability jump towards lower temperatures with decreasing metallicity.

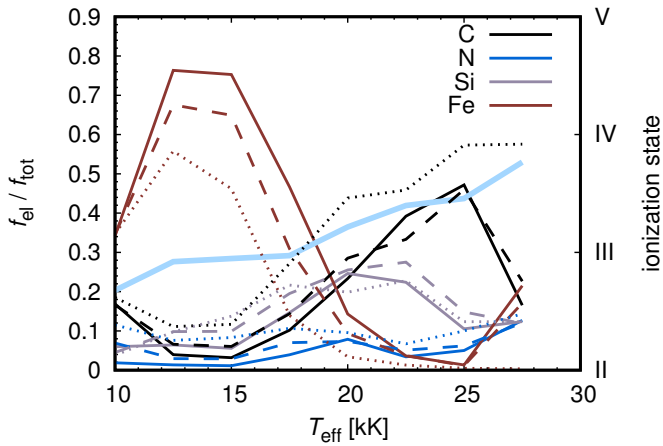


Fig. 2. Relative contribution of selected elements to the line radiative force as a function of the effective temperature of a model star, plotted at the wind critical point for models with $M = 40 M_{\odot}$. Different line styles denote metallicity, with the solid line corresponding to Z_{\odot} , dashed line to $0.5Z_{\odot}$, and dotted line to $0.2Z_{\odot}$. The thick blue line (with corresponding axis on the right) plots the mean ionization state driving the wind for metallicity $0.5Z_{\odot}$. This is defined as $\sum f_i z_i / (\sum f_i)$, where f_i is the contribution of ion i with charge z_i to the line radiative force. For simplicity, the values were obtained within the Sobolev approximation.

4. Tests against observations and comparison with independent theoretical models

While the wind mass-loss rates can be determined from manifold observables spanning almost the entire electromagnetic domain in our Galaxy, the choice is significantly constrained in nearby galaxies. Typically, only mass-loss rates from optical hydrogen emission lines are available, supplemented in rare cases with mass-loss rates from UV wind lines. This significantly complicates any comparison with theoretical predictions because of the influence of clumping. While estimates from UV regions can be independently corrected for clumping (Ramachandran et al. 2019; Bouret et al. 2021), the estimates based on optical data are overestimated by a factor of a few, which depends on the strength of clumping (expressed by C_c , Puls et al. 2008). Moreover, while observational studies typically account for optically thin clumping at most, allowing for optically thick clumps provides results that are more robust (Šurlan et al. 2013).

This is reflected in the comparison of theoretical predictions with observational data in Fig. 3. Here, we plot the ratio of mass-loss rates determined from observations to those predicted for individual stars. For mass-loss rates derived from optical emission lines, the ratio is always higher than one, which indicates that the theory does not contradict observations. Quantitatively, the mass-loss rates determined from optical emission lines are higher than predictions by factors of, on average, 6.4 and 6.0 for the LMC and SMC, respectively. Considering the proportionality of predicted mass-loss rates, $\dot{M} \sim C_c^{0.06}$, and the dependence of clumping corrections via $\dot{M} \sim C_c^{-0.5}$ (e.g., Puls et al. 2008), the theory agrees with observations for $C_c = 28$ for the LMC and for $C_c = 25$ for the SMC. These are slightly higher values than those obtained from observational studies of SMC stars (Bouret et al. 2021). On the other hand, these values are close to $C_c = 24$, which is the value derived for Galactic supergiants (Krtićka et al. 2021), and agree with theory and observations showing that the (optically thin) clumping factor is almost independent of metallicity (Brands et al. 2022; Driessen et al. 2022).

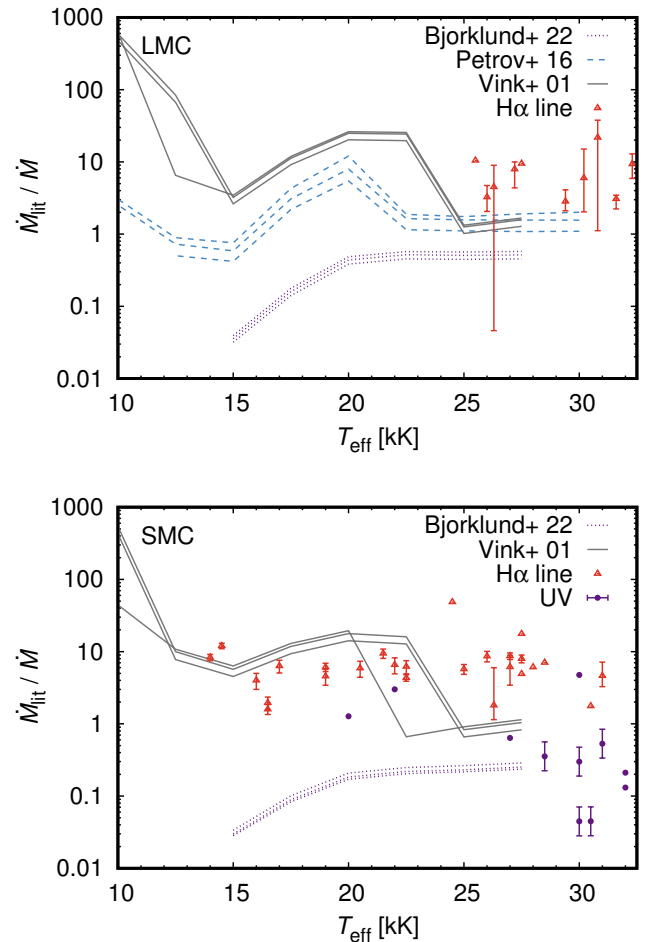


Fig. 3. Ratio of mass-loss rates derived from the literature and mass-loss rates predicted using Eq. (3) plotted as a function of effective temperature for stars from the LMC (*Upper panel*) and SMC (*Lower panel*). The observational values include mass-loss rates determined from the Balmer lines (mostly $H\alpha$ line, red triangles, Evans et al. 2004; Trundle et al. 2004; Trundle & Lennon 2005; Mokiem et al. 2006, 2007), and from UV wind lines corrected for clumping (violet dots, Ramachandran et al. 2019; Bouret et al. 2021). Overplotted are theoretical predictions evaluated for stellar parameters from our sample (Vink et al. 2001; Björklund et al. 2023) (solid gray and dotted purple lines, respectively) and for parameters of Petrov et al. (2016) (dashed blue lines).

The theoretical predictions of mass-loss rates agree better with estimates from UV lines (and $H\alpha$ in some cases) corrected for optically thin clumping. On average, the theoretical predictions are by a factor of 2.5 higher than values from observations. However, this comparison is perhaps influenced by the so-called "weak wind problem", which relates to the weak wind lines in the spectra of late O stars (Bouret et al. 2003; Martins et al. 2004). This effect is considered to be caused by slow cooling of wind material in post-shock regions (Cohen et al. 2008; Krtićka & Kubát 2009; Lagae et al. 2021). Moreover, some of the stars analyzed by Ramachandran et al. (2019) are main sequence stars, for which we have to extrapolate in Eq. (3).

If the effect of clumping on observations is neglected, predictions of Vink et al. (2001) underestimate the mass-loss rates for early B SMC supergiants and overestimate them for mid B supergiants (Trundle et al. 2004). This can be seen in Fig. 3, where we also plot the ratio of Vink et al. (2001) predictions to our

predictions for stars from our sample (Table 1). The Vink et al. (2001) predictions are plotted for a terminal-to-escape-speed ratio of 2.6 above the bistability jump and 1.3 below the jump, respectively. Above the jump and for higher v_∞/v_{esc} ratios and low metallicities, these predictions reasonably agree with ours, although there is significant disagreement for higher metallicities or higher effective temperatures (Krtićka & Kubát 2017; Krtićka et al. 2021). This leads us to the conclusion that the differences between the rates of Vink et al. (2001) and ours are caused mostly by the treatment of iron lines, which do not significantly contribute to the line driving for B supergiants at low metallicities and above the bistability jump (Fig. 2). However, the bistability jump predicted by Vink et al. (2001) is stronger than ours, resulting in greater disagreement in predicted rates below about 22.5 kK. The very large disagreement between our rates and the predictions of Vink et al. (2001) around $T_{\text{eff}} \approx 10$ kK (Fig. 3) is connected to the appearance of the second bistability jump, which is due to recombination of Fe III. This is the main reason why the values of mass-loss rates differ so markedly at the lower T_{eff} boundary of our grid. In the CMFGEN (Hillier & Miller 1998) models provided by Petrov et al. (2016), the recombination appears at lower temperatures, around $T_{\text{eff}} \approx 9$ kK. Also, in our models, Fe III dominates at the critical point, where the mass-loss rate is determined.

While our mass-loss rate predictions agree reasonably well with the theoretical calculations of Björklund et al. (2023) for solar metallicities, they are by a factor of a few higher at lower metallicities (Fig. 3). The agreement is even worse in the region below the temperature of the bistability jump. The bistability jump is missing in Björklund et al. (2023). Except in the region of the bistability jump around 17.5 kK, our predictions agree nicely with the calculations of Petrov et al. (2016), which are based on the CMFGEN code.

Observational analysis of terminal velocities provides another test of stellar wind theory. Wind terminal velocity is typically studied in terms of the temperature dependence of the terminal-velocity-to-escape-speed ratio (Lamers et al. 1995; Crowther et al. 2006). However, this relationship shows relatively large scatter. Terminal velocities can also be conveniently tested in terms of their dependence on the effective temperature (Hawcroft et al. 2023), which also reflects the evolution of stars. We used a large sample of terminal velocity measurements of SMC and LMC OB supergiants obtained from the ULLYSES project (Roman-Duval et al. 2020; Vink et al. 2023) by Hawcroft et al. (2023). These values are compared with predictions obtained here and by Krtićka et al. (2021).

The plot (Fig. 4) shows an increase in terminal velocity with temperature, which stems from the scaling of terminal velocity with escape speed and from the decreasing escape speed in the course of stellar evolution. These trends are nicely reproduced by our models, in which the relationship between the stellar effective temperature, mass, and luminosity reflects the evolution of stars.

The models can also be tested against observations of stars residing in galaxies from the Local Group. Urbaneja et al. (2003) derived wind parameters for two early B-type supergiants with $Z = 1.0$ and $Z = 0.3$ in the Sculptor galaxy NGC 300 from optical spectroscopy. The derived mass-loss rates are higher than those predicted using Eq. (3) by a factor of about 10. This factor corresponds to the level of clumping found in other B supergiants. On the other hand, the terminal velocities determined from observations nicely correspond to theoretical predictions. A similar discrepancy of a factor of about 5 in mass-loss rates can be found from optical analysis of M33 supergiants

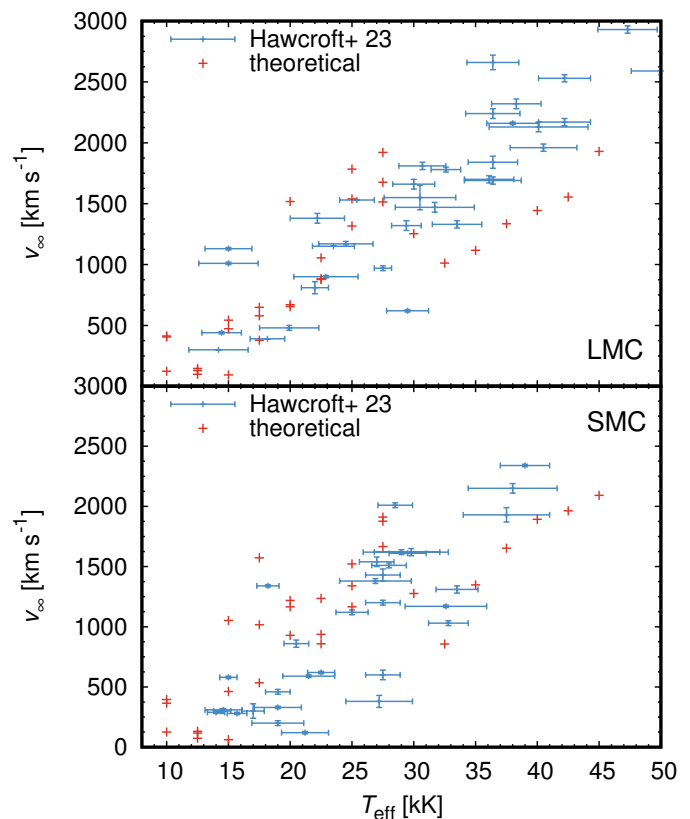


Fig. 4. Terminal velocities of OB supergiants from the LMC (*upper panel*) and SMC (*lower panel*) as a function of temperature (Hawcroft et al. 2023) in comparison with our theoretical values.

(Urbaneja et al. 2005, with $Z = 0.3 - 1.0$), again neglecting the influence of clumping.

To roughly check our models with observations, in Fig. 5 we provide the spectra of selected B supergiants from the LMC and SMC in the region of strong wind lines observed by HST via the ULLYSES program (Roman-Duval et al. 2020) and downloaded from the publicly available MAST archive¹. We chose stars that have parameters listed in Hawcroft et al. (2023) that are close in value to their counterparts in the calculated models from our grid (Table 1). This series of spectra show strengthening of wind lines towards higher effective temperatures, which is nicely reproduced by the models. Some features are not fully reproduced because of missing physics, such as the neglect of small-scale structures (Sundqvist et al. 2010; Šurlan et al. 2012) or X-ray emission (Carneiro et al. 2016; Bernini-Peron et al. 2023), but the overall agreement is reasonable.

5. Discussion

The present paper provides further support for the downward revision of mass-loss rate predictions in hot massive stars (Krtićka & Kubát 2017; Sundqvist et al. 2019; Gormaz-Matamala et al. 2022). Together with observational indications of lower mass-loss rates in massive stars (e.g., Šurlan et al. 2013; Kobulnicky et al. 2019; Brands et al. 2022), this challenges our current understanding of massive star evolution. Although lower mass-loss rates might be favorable for the

¹ <https://mast.stsci.edu/search/ui/#/ullyses>

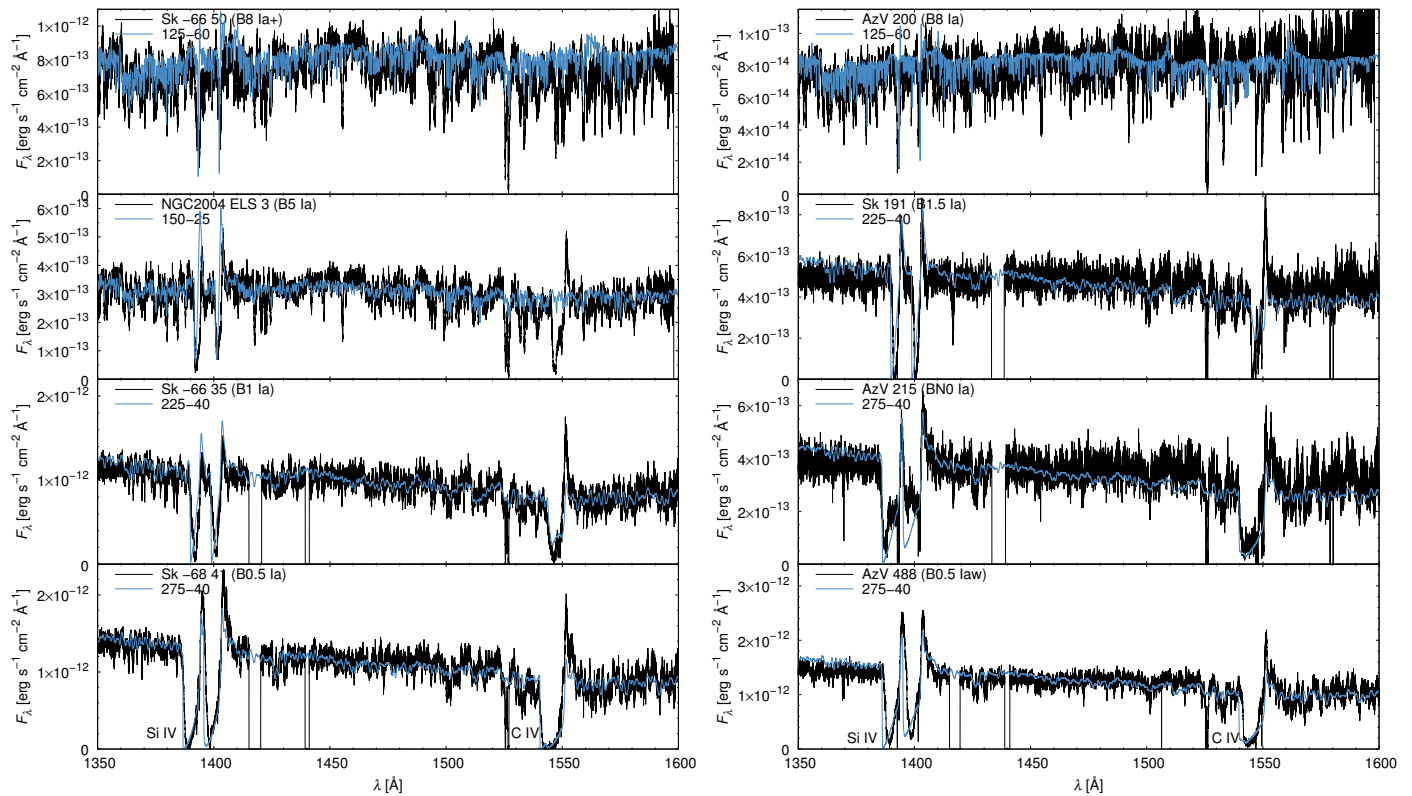


Fig. 5. Comparison of the spectra of selected B supergiants (black lines) with the emergent spectra of model stars (blue lines) from the grid for the LMC (left panel) and SMC (right panel).

solution of particular problems, such as the overly heavy masses of merging black holes (Abbott et al. 2016; Groh et al. 2020), they may give rise to other discrepancies.

On the other hand, line-driven winds might not form a dominant constituent of the total stellar mass loss. For instance, evolutionary models of a solar-metallicity star with an initial mass of $60 M_{\odot}$ predict that more than half of the stellar mass is lost before the star enters the Wolf-Rayet stage (Groh et al. 2014). However, only about one-third of the mass loss happens during OB phases, the rest appears during the luminous blue variable (LBV) stage. Evolved stars, such as LBVs, may lose mass by other mechanisms (Sanyal et al. 2015; Owocki et al. 2019). In a similar way, the red supergiant phase may be important for total mass loss in stars with lower initial mass (Renzo et al. 2017).

There are other observables that can be used to test the influence of mass loss on stellar evolution; for instance, the distribution of observed rotational velocities and the corresponding angular momentum loss (Keszthelyi et al. 2017). Mass loss also modifies stellar radii and luminosities (Gormaz-Matamala et al. 2022). The strength of interaction between massive stars and surrounding circumstellar environment depends on the wind mass-loss rate, but numerical simulations show that the effects due to winds only dominate over the influence of ionizing flux in very dense clouds close to the stars (Dale et al. 2013). Weaker line driving leads to weaker ablation of circumstellar discs (Kee et al. 2016), which could be one of the effects behind the appearance of relatively early Oe stars in the SMC (Golden-Marx et al. 2016).

6. Conclusions

We provide global hydrodynamical models of line-driven winds in B supergiants from the Large and Small Magellanic Clouds.

The velocity and density structure of the models is determined using radiative force calculated from the solution of the radiative transfer equation in the comoving frame using level populations derived from kinetic equilibrium equations. The models are calculated in a global manner, that is, we solve structural equations from nearly hydrostatic atmosphere to supersonically expanding radiatively driven wind. The models are parameterized by basic stellar parameters, which are effective temperature, radius, mass, and metallicity.

Predicted wind mass-loss rates scale with metallicity on average as $\dot{M} \sim Z^{0.60}$ and are proportional to the stellar luminosity. Mass-loss rates are sensitive to stellar effective temperature; they significantly increase in the region of the so-called bistability jump at about 20 kK. However, the variations at this temperature do not resemble a steep jump, but are rather continuous and appear due to recombination of Fe IV to Fe III. Moreover, the strength of the jump weakens towards lower metallicities.

We provide a formula expressing predicted mass-loss rates in terms of basic stellar parameters. At metallicities corresponding to those found in the Magellanic Clouds and for temperatures above the bistability jump, this formula provides similar rates to those used in current evolutionary models. However, our predictions are significantly lower than those of Vink et al. (2001) below the bistability jump. We compare our predictions with observational estimates derived from the H α line. Above the bistability jump, H α mass-loss rate estimates for stars from the Galaxy and Magellanic Clouds agree with theoretical predictions assuming a single clumping factor of about 25. Our models nicely reproduce the observational dependence of terminal velocity on temperature derived from UV spectroscopy and provide spectra that reasonably agree with observations.

Acknowledgements. Computational resources were provided by the e-INFRA CZ project (ID:90254), supported by the Ministry of Education, Youth and Sports of the Czech Republic. The Astronomical Institute Ondřejov is supported by a project RVO:67985815 of the Academy of Sciences of the Czech Republic.

References

- Abbott, B. P., Abbott, R., Abbott, T. D., et al. 2016, *ApJ*, 818, L22
- Asplund, M., Grevesse, N., Sauval, A. J., & Scott, P. 2009, *ARA&A*, 47, 481
- Battaglia, G., Taibi, S., Thomas, G. F., & Fritz, T. K. 2022, *A&A*, 657, A54
- Bernini-Peron, M., Marcolino, W. L. F., Sander, A. A. C., et al. 2023, *A&A*, 677, A50
- Björklund, R., Sundqvist, J. O., Puls, J., & Najarro, F. 2021, *A&A*, 648, A36
- Björklund, R., Sundqvist, J. O., Singh, S. M., Puls, J., & Najarro, F. 2023, *A&A*, 676, A109
- Bouret, J.-C., Hillier, D. J., Lanz, T., & Fullerton, A. W. 2012, *A&A*, 544, A67
- Bouret, J.-C., Lanz, T., Hillier, D. J., et al. 2003, *ApJ*, 595, 1182
- Bouret, J. C., Martins, F., Hillier, D. J., et al. 2021, *A&A*, 647, A134
- Brands, S. A., de Koter, A., Bestenlehner, J. M., et al. 2022, *A&A*, 663, A36
- Carneiro, L. P., Puls, J., Sundqvist, J. O., & Hoffmann, T. L. 2016, *A&A*, 590, A88
- Castor, J. I., Abbott, D. C., & Klein, R. I. 1975, *ApJ*, 195, 157
- Castor, J. I., Abbott, D. C., & Klein, R. I. 1976, in *Physique des Mouvements dans les Atmospheres*, ed. R. Cayrel & M. Steinberg (Paris: CNRS), 363–393
- Cohen, D. H., Kuhn, M. A., Gagné, M., Jensen, E. L. N., & Miller, N. A. 2008, *MNRAS*, 386, 1855
- Crowther, P. A., Lennon, D. J., & Walborn, N. R. 2006, *A&A*, 446, 279
- Dale, J. E., Ngoumou, J., Ercolano, B., & Bonnell, I. A. 2013, *MNRAS*, 436, 3430
- Driessen, F. A., Sundqvist, J. O., & Dagore, A. 2022, *A&A*, 663, A40
- Evans, C. J., Crowther, P. A., Fullerton, A. W., & Hillier, D. J. 2004, *ApJ*, 610, 1021
- Feldmeier, A. & Thomas, T. 2017, *MNRAS*, 469, 3102
- Flores, B. L., Hillier, D. J., & Dessart, L. 2023, *MNRAS*, 518, 5001
- Gayley, K. G. 1995, *ApJ*, 454, 410
- Golden-Marx, J. B., Oey, M. S., Lamb, J. B., Graus, A. S., & White, A. S. 2016, *ApJ*, 819, 55
- Gormaz-Matamala, A. C., Curé, M., Meynet, G., et al. 2022, *A&A*, 665, A133
- Gräfener, G. & Hamann, W.-R. 2008, *A&A*, 482, 945
- Groh, J. H., Farrell, E. J., Meynet, G., et al. 2020, *ApJ*, 900, 98
- Groh, J. H., Meynet, G., Ekström, S., & Georgy, C. 2014, *A&A*, 564, A30
- Hamann, W. R. & Koesterke, L. 1998, *A&A*, 335, 1003
- Hawcroft, C., Sana, H., Mahy, L., et al. 2023, arXiv e-prints, arXiv:2303.12165
- Hill, V., Andrievsky, S., & Spite, M. 1995, *A&A*, 293, 347
- Hillier, D. J. & Miller, D. L. 1998, *ApJ*, 496, 407
- Hummer, D. G., Berrington, K. A., Eissner, W., et al. 1993, *A&A*, 279, 298
- Kee, N. D., Owocki, S., & Sundqvist, J. O. 2016, *MNRAS*, 458, 2323
- Keszthelyi, Z., Puls, J., & Wade, G. A. 2017, *A&A*, 598, A4
- Kobulnicky, H. A., Chick, W. T., & Povich, M. S. 2019, *AJ*, 158, 73
- Kramida, A., Ralchenko, Y., Reader, J., & NIST ASD Team. 2015, NIST Atomic Spectra Database, <https://www.nist.gov/pml/atomic-spectra-database>, [Online]
- Krtićka, J. & Kubát, J. 2006, *A&A*, 446, 1039
- Krtićka, J. & Kubát, J. 2009, *MNRAS*, 394, 2065
- Krtićka, J. & Kubát, J. 2011, *A&A*, 534, A97
- Krtićka, J. & Kubát, J. 2017, *A&A*, 606, A31
- Krtićka, J. & Kubát, J. 2018, *A&A*, 612, A20
- Krtićka, J., Kubát, J., & Krtićková, I. 2018, *A&A*, 620, A150
- Krtićka, J., Kubát, J., & Krtićková, I. 2021, *A&A*, 647, A28
- Krtićka, J., Owocki, S. P., Kubát, J., Galloway, R. K., & Brown, J. C. 2003, *A&A*, 402, 713
- Lagae, C., Driessen, F. A., Hennicker, L., Kee, N. D., & Sundqvist, J. O. 2021, *A&A*, 648, A94
- Lamers, H. J. G. L. M., Snow, T. P., & Lindholm, D. M. 1995, *ApJ*, 455, 269
- Lanz, T. & Hubeny, I. 2003, *ApJS*, 146, 417
- Lanz, T. & Hubeny, I. 2007, *ApJS*, 169, 83
- Martins, F., Schaerer, D., Hillier, D. J., & Heydari-Malayeri, M. 2004, *A&A*, 420, 1087
- Martins, F., Schaerer, D., Hillier, D. J., et al. 2005, *A&A*, 441, 735
- Massana, P., Ruiz-Lara, T., Noël, N. E. D., et al. 2022, *MNRAS*, 513, L40
- Mihalas, D., Kunasz, P. B., & Hummer, D. G. 1975, *ApJ*, 202, 465
- Milne, E. A. 1926, *MNRAS*, 86, 459
- Mokiem, M. R., de Koter, A., Evans, C. J., et al. 2007, *A&A*, 465, 1003
- Mokiem, M. R., de Koter, A., Evans, C. J., et al. 2006, *A&A*, 456, 1131
- Najarro, F., Figuer, D. F., Hillier, D. J., Geballe, T. R., & Kudritzki, R. P. 2009, *ApJ*, 691, 1816
- Najarro, F., Hanson, M. M., & Puls, J. 2011, *A&A*, 535, A32
- Owocki, S. P., Hirai, R., Podsiadlowski, P., & Schneider, F. R. N. 2019, *MNRAS*, 485, 988
- Patel, E., Besla, G., & Sohn, S. T. 2017, *MNRAS*, 464, 3825
- Pauldrach, A. W. A. & Puls, J. 1990, *A&A*, 237, 409
- Petrov, B., Vink, J. S., & Gräfener, G. 2016, *MNRAS*, 458, 1999
- Puls, J., Markova, N., Scuderi, S., et al. 2006, *A&A*, 454, 625
- Puls, J., Springmann, U., & Lennon, M. 2000, *A&AS*, 141, 23
- Puls, J., Vink, J. S., & Najarro, F. 2008, *A&A Rev.*, 16, 209
- Ramachandran, V., Hamann, W. R., Oskinova, L. M., et al. 2019, *A&A*, 625, A104
- Renzo, M., Ott, C. D., Shore, S. N., & de Mink, S. E. 2017, *A&A*, 603, A118
- Rolleston, W. R. J., Trundle, C., & Dufton, P. L. 2002, *A&A*, 396, 53
- Roman-Duval, J., Proffitt, C. R., Taylor, J. M., et al. 2020, *Research Notes of the American Astronomical Society*, 4, 205
- Sander, A. A. C., Hamann, W.-R., Todt, H., Hainich, R., & Shenar, T. 2017, *A&A*, 603, A86
- Sanyal, D., Grassitelli, L., Langer, N., & Bestenlehner, J. M. 2015, *A&A*, 580, A20
- Seaton, M. J., Zeippen, C. J., Tully, J. A., et al. 1992, *Rev. Mexicana Astron. Astrofis.*, 23, 19
- Springmann, U. W. E. & Pauldrach, A. W. A. 1992, *A&A*, 262, 515
- Sundqvist, J. O., Björklund, R., Puls, J., & Najarro, F. 2019, *A&A*, 632, A126
- Sundqvist, J. O., Owocki, S. P., & Puls, J. 2018, *A&A*, 611, A17
- Sundqvist, J. O., Puls, J., & Feldmeier, A. 2010, *A&A*, 510, A11
- Szécsi, D. & Wünsch, R. 2019, *ApJ*, 871, 20
- Trundle, C. & Lennon, D. J. 2005, *A&A*, 434, 677
- Trundle, C., Lennon, D. J., Puls, J., & Dufton, P. L. 2004, *A&A*, 417, 217
- Urbaneja, M. A., Herrero, A., Bresolin, F., et al. 2003, *ApJ*, 584, L73
- Urbaneja, M. A., Herrero, A., Kudritzki, R. P., et al. 2005, *ApJ*, 635, 311
- Šurlan, B., Hamann, W.-R., Aret, A., et al. 2013, *A&A*, 559, A130
- Šurlan, B., Hamann, W.-R., Kubát, J., Oskinova, L. M., & Feldmeier, A. 2012, *A&A*, 541, A37
- Venn, K. A. 1999, *ApJ*, 518, 405
- Vink, J. S. 2018, *A&A*, 619, A54
- Vink, J. S., de Koter, A., & Lamers, H. J. G. L. M. 1999, *A&A*, 350, 181
- Vink, J. S., de Koter, A., & Lamers, H. J. G. L. M. 2001, *A&A*, 369, 574
- Vink, J. S., Mehner, A., Crowther, P. A., et al. 2023, *A&A*, 675, A154
- Vink, J. S. & Sander, A. A. C. 2021, *MNRAS*, 504, 2051
- Weisz, D. R., Dolphin, A. E., Skillman, E. D., et al. 2013, *MNRAS*, 431, 364